










## Advancing Precision Particle Background Estimation for Future X-ray Missions: Correlated Variability between AMS and Chandra/XMM-Newton

ARNAB SARKAR <sup>1</sup>, CATHERINE E. GRANT <sup>1</sup>, ERIC D. MILLER <sup>1</sup>, MARK BAUTZ <sup>1</sup>, BENJAMIN SCHNEIDER <sup>1</sup>,  
RICK F. FOSTER,<sup>1</sup> GERRIT SCHELLENBERGER <sup>2</sup>, STEVEN ALLEN <sup>3</sup>, RALPH P. KRAFT <sup>2</sup>, DAN WILKINS <sup>3</sup>,  
ABE FALCONE,<sup>4</sup> AND ANDREW PTAK<sup>5</sup>

<sup>1</sup>MIT Kavli Institute for Astrophysics and Space Research, 70 Vassar St, Cambridge, MA 02139, USA

<sup>2</sup>Center for Astrophysics | Harvard & Smithsonian, 60 Garden st, Cambridge, MA 02139, USA

<sup>3</sup>Stanford University, 382 Via Pueblo Mall, Stanford, California 94305, USA

<sup>4</sup>Pennsylvania State University, 0525 Davey Laboratory, University Park, PA 16802, USA

<sup>5</sup>NASA Goddard Space Flight Center, Greenbelt, MD20771, USA

### ABSTRACT

Galactic cosmic ray (GCR) particles have a significant impact on the particle-induced background of X-ray observatories, and their flux exhibits substantial temporal variability, potentially influencing background levels. In this study, we present one-day binned high-energy reject rates derived from the Chandra-ACIS and XMM-Newton EPIC-pn instruments, serving as proxies for GCR particle flux. We systematically analyze the ACIS and EPIC-pn reject rates and compare them with the AMS proton flux. Our analysis initially reveals robust correlations between the AMS proton flux and the ACIS/EPIC-pn reject rates when binned over 27-day intervals. However, a closer examination reveals substantial fluctuations within each 27-day bin, indicating shorter-term variability. Upon daily binning, we observe finer temporal structures in the datasets, demonstrating the presence of recurrent variations with periods of  $\sim 25$  days and 23 days in ACIS and EPIC-pn reject rates, respectively, spanning the years 2014 to 2018. Notably, during the 2016–2017 period, we additionally detect periodicities of  $\sim 13.5$  days and 9 days in the ACIS and EPIC-pn reject rates, respectively. Intriguingly, we observe a time lag of  $\sim 6$  days between the AMS proton flux and the ACIS/EPIC-pn reject rates during the second half of 2016. This time lag is not visible before 2016 and after 2017. The underlying physical mechanisms responsible for this time lag remain a subject of ongoing investigation.

### 1. INTRODUCTION

Athena (Advanced Telescope for High ENergy Astrophysics), ESA’s next large X-ray observatory, is scheduled to launch in the mid 2030s to Earth-Sun L2 (Nandra et al. 2013). Some of Athena’s primary scientific objectives align with the study of faint diffuse emission, including those from galaxy clusters, groups of galaxies, and the intergalactic medium (IGM). These are also primary science goals of current (e.g., Chandra, XMM-Newton, eROSITA, XRISM) and future (Lynx; Gaskin et al. 2019, LEM; Kraft et al. 2022, AXIS; Reynolds et al. 2023) X-ray telescopes. Achieving these objectives hinges on precise control of the total flux and minimizing systematic uncertainties linked to our understanding of the non-X-ray background (Sarkar et al. 2021,

2022a,b, 2023, 2024). Extensive efforts have been invested in understanding, modeling, and mitigating this background component originating from particles and high-energy photons, for example, the Self-Anti-Coincidence (SAC) technique, Miller et al. 2022, machine learning approach, Poliszczuk et al. 2023, and many others (e.g., Grant et al. 2018; Bulbul et al. 2020; Grant et al. 2022; Gastaldello et al. 2022). The non-X-ray background has consistently posed a significant challenge in X-ray missions, limiting the full exploitation of scientific data from diffuse sources (Molendi 2017).

The non-X-ray background arises primarily from two sources: soft protons focused onto the focal plane by the telescope mirrors and unfocused background generated by various particles (Campana 2022). Soft protons, originating in the solar corona and Earth’s magnetosphere, possess energies typically below a few 100 keV and can reach the detectors due to their concentration by the telescope mirrors. The spectral shape of this

component can be approximated by a power-law continuum, characterized by highly variable intensity and slope (Kuntz & Snowden 2008). Soft protons, when present, can dramatically elevate the overall background intensity in brief time intervals, often referred to as “soft proton flares” (Kuntz & Snowden 2008). These protons primarily deposit their energy near the detector’s surface and generate event patterns identical to valid X-ray photons, making them challenging to distinguish and reject during onboard processing (Gastaldello et al. 2017).

The unfocused particle-induced background can arise from several sources, including Galactic cosmic rays (GCRs), solar energetic protons, and trapped radiation within Earth’s magnetosphere. The characteristics of this background, including its temporal behavior, spectral features, and spatial distribution, depend on the primary particle’s energy. GCR particles, typically with energies greater than 10 MeV and composed mainly of protons, electrons, and helium ions, exhibit variability linked to the solar cycle. These incoming particles interact with the detector and surrounding components, giving rise to secondary particles (e.g., Kuntz & Snowden 2008; von Kienlin et al. 2018). To prevent these high-energy particles from saturating the limited bandwidth for telemetry, onboard event processing is employed to reject events generated by primary GCRs, primarily due to their high total energies or their distinctive pixel patterns (Lumb et al. 2002). However, secondary electrons and photons resulting from these unfocused components deposit charge in the detector, posing challenges in distinguishing them from X-ray events originating from celestial sources. Consequently, they significantly contribute to, and often dominate, the residual (unrejected) instrumental background.

Quantifying the particle-induced background of X-ray observatories is a complex task due to its pronounced temporal variability, further complicated by the presence or absence of the geomagnetic shielding. The transportation of GCRs within the heliosphere is governed by the interplay between the solar wind and the regular as well as turbulent components of the heliospheric magnetic field (HMF). As GCRs interact with the solar wind and the HMF, their spectrum below a few dozen GV undergoes modulation relative to the local interstellar spectrum (LIS; Potgieter 2013). This modulation of GCR flux leads to a range of quasi-periodic variations occurring on various timescales, spanning from hours to several years. These phenomena have been extensively studied in Usoskin (2017); Kudela & Sabbah (2016); Chowdhury et al. (2016); Bazilevskaya et al. (2014); Modzelewska & Gil (2021) and references therein.

GCR particles are routinely detected and characterized using the Alpha Magnetic Spectrometer (AMS-02) instrument, a specialized particle detector installed on the International Space Station (ISS) (Kounine 2012; Aguilar et al. 2015). AMS provides precise, synoptic measurements of GCR particle fluxes and energies on timescales as short as 1 day (Aguilar et al. 2021). These data, when compared to background rates measured aboard X-ray observatories can provide insight into the mechanisms responsible for level and variability of the particle-induced background in X-ray instruments.

When a GCR particle interacts with an X-ray detector, it leaves behind a distinctive particle track marked by multiple pixels with large signal charge. Various X-ray telescopes employ specific algorithms to identify such invalid (i.e. non-X-ray) events.

These algorithms exploit the fact that X-ray optics focus incident cosmic X-rays over a limited spectral band with a well-defined upper energy limit. Thus, for instance, the ACIS instrument onboard Chandra has an on-board filter that rejects events with energies surpassing a designated threshold. Similarly, the EPIC-pn instrument onboard XMM-Newton discards entire columns of pixels that contain pixels with energies exceeding a predefined threshold. Although these detectors do not directly measure GCR particle fluxes, the count of discarded events, expressed as reject rates per frame per frame time, can serve as a proxy measurement of GCR particle fluxes, as shown in several previous studies (Grant et al. 2018; Bulbul et al. 2020; Gastaldello et al. 2022). Notably, Grant et al. (2022) demonstrated a strong correlation between AMS proton fluxes and ACIS reject rates binned over 27-day intervals, further affirming the efficacy of X-ray reject rates as proxies for GCR particle fluxes.

Despite the critical relevance of the variabilities seen in the GCR particle flux (Aguilar et al. 2021), their impact on the variability of the particle background as seen by X-ray detectors has been relatively unexplored, primarily due to the limited availability of non-X-ray-background information over long intervals at fine time bin. In this paper, for the first time we present results derived from the analysis of one-day binned ACIS and EPIC-pn reject rates, encompassing data from nearly all archival science observations spanning the years 2011–2020. We examine the long-term and short-term variabilities in both datasets and compare them with that of AMS proton fluxes. We discuss how this knowledge can inform future missions, by inclusion of special purpose particle monitors, or by comparison to other space-based particle monitors. The overarching objective of this work is to enhance our understanding of instrumental

background characterization and mitigation strategies, particularly relevant to the Athena Wide-Field Imager (WFI). Results of this work, however, can be extended and applied to any future X-ray missions.

## 2. DATA GATHERING

GCR protons are one of the important sources of quiescent particle-background, modulated by the solar cycle and solar activity. We analyze 9 years (2011–2020) of archival data on proton flux and high-energy reject rates from AMS, Chandra, and XMM-Newton.

### 2.1. *Alpha Magnetic Spectrometer (AMS-02)*

The AMS-02 (hereafter AMS) is a state-of-the-art particle physics experiment module installed on the ISS in May 2011. Developed to explore the cosmos for high-energy cosmic rays and particles, the AMS plays a crucial role in advancing our understanding of fundamental physics phenomena. This sophisticated instrument is equipped with permanent magnet, silicon tracker and time of flight (TOF) scintillation counters that allow it to identify and analyze the properties of cosmic particles with unparalleled precision (Aguilar et al. 2015). For the detailed layout of the detector, we refer readers to Kounine (2012). The large acceptance and high precision of the AMS allow it to perform accurate measurements of the particle fluxes as functions of time and energy. Its unique vantage point in space provides data that cannot be easily obtained from Earth-based experiments, providing unique opportunities to probe the dynamics of solar modulation (Tomassetti 2017), and the GCR propagation (Boschini et al. 2017).

Though AMS orbits in Low Earth Orbit (LEO), proton flux measured by AMS can be reconstructed to anticipate the flux that would occur in the absence of Earth’s magnetic field shielding (Kounine 2012; Aguilar et al. 2015). By understanding the ISS’s path around the Earth, the observed cosmic ray spectrum can be corrected for the effects of geomagnetic shielding at each point in the ISS orbit to obtain the spectrum incident outside the Earth’s magnetosphere (Aguilar et al. 2015). Since the ISS’s orbital journey exposes it to varying levels of cut-off rigidity, the GCR proton spectrum can be reconstructed as without the influence of Earth’s magnetic field. The AMS team has successfully accomplished this reconstruction, including assessments of the potential errors introduced by this process, as well as by the other calibration and filtering procedures and made this data available to the wider community (Aguilar et al. 2015, 2021).

Regarding the GCR proton flux, there have been three significant data releases in the literature by the AMS

team. Firstly, the precise measurement of the proton spectrum conducted by Aguilar et al. (2015). Following that, an investigation into the temporal patterns of proton fluxes on timescales of the Bartels rotation period (a period of 27 days, approximately equivalent to the synodic solar rotation period), as detailed in Aguilar et al. (2018). Lastly, Aguilar et al. (2021) presents the daily variations in proton fluxes. In the scope of our current research, we employ these meticulously calibrated daily proton flux data spanning from 2011 to 2019. For this work, we summed all the proton fluxes in the 0.4–60 GeV energy band for a specific time bin. This dataset enables us to examine the temporal intricacies of GCR protons while considering the particle background effects relevant to future X-ray telescopes.

### 2.2. *Chandra ACIS*

The Advanced CCD Imaging Spectrometer (ACIS) onboard the Chandra X-ray Observatory was launched into a highly elliptical 2.7 day orbit in 1999. ACIS employs an assembly of framestore charge-coupled devices (CCDs), comprising a total of ten CCDs. Each individual CCD encompasses a matrix of 1024 by 1024 pixels, each with dimensions of 24 microns. Our particular focus centers on the properties of the back-illuminated (BI) CCD, specifically ACIS-S3, situated at the ACIS-S aimpoint (Grant et al. 2022). This choice is motivated by its intrinsic resemblance to forthcoming detectors such as the Athena-WFI. ACIS-S3 measures 45 microns in thickness, operates in a fully depleted state, and is configured for photon-counting mode, characterized by frametimes of approximately 3 seconds. For detailed layout we refer readers to Weisskopf et al. (2000).

Chandra is in a highly elliptical orbit (perigee  $\sim$  10,000 km; apogee  $\sim$  130,000 km) which traverses diverse particle environments during its orbital trajectory, dipping into the Earth’s radiation belts around perigee. Scientific observations, however, all occur well outside Earth’s radiation belts and magnetic shielding at altitudes above roughly 60,000 km (Grant et al. 2002). The Chandra orbit evolves with time with apogee ranging from about 130,000 to 145,000 km during this time period. It is anticipated that the external particle environment encountered by potential upcoming missions at the Lagrange points L1/L2 or in other high-Earth orbits should closely resemble that observed by Chandra. This similarity underscores the significance of ACIS as a valuable tool for investigating high-energy GCR particles and comprehending their impact on particle background dynamics.

The detection methodology involves an on-board filtering mechanism: events with pulse-heights surpassing

a tunable upper threshold (generally either 13 keV or 15 keV), as well as events exhibiting morphologies characterized by an abundance of contiguous pixels, are systematically excluded. While the filtered events are not telemetered to the ground, the instrument maintains a comprehensive record of the count of eliminated events and the rationale behind their removal. Among these counters, the parameter denoted as the “high-energy reject rate” serves as a proxy <sup>\*</sup> for the particle rate encountered by the spacecraft.

In this study, we investigate high-energy reject rates (reject rates hereafter) from the period spanning 2011 to 2020. These rates are available in the standard data products provided with each ACIS observation. <sup>†</sup> In this particular study, we made use of a separate telemetry archive created by the ACIS instrument team, as a quicker method to access the reject rates. To derive the reject rates, we employ two distinct datasets.

One set of data with a threshold of 3750 ADU ( $\sim 15$  keV) was collected during instances when ACIS was in a stowed configuration and was exposed to an external calibration source. During this configuration, the detector remained shielded from focused X-rays. Another set of data with a threshold of 3275 ADU ( $\sim 13$  keV) was gathered during the time when detector was exposed to the sky for nominal science operation. The reject rates were derived by aligning the 15 keV dataset with the 13 keV dataset and combining them. To achieve this alignment, the 15 keV dataset was normalized using the best-fit parameters derived from a linear regression analysis between the two datasets. Figure 1 provides a visualization of these datasets along with their corresponding best-fit linear regression line.

It is worth noting that the prevailing quiescent particle background primarily arises from GCR protons and any secondary particles from interactions with the spacecraft and instrument components, whether the instrument is in the stowed position or otherwise. Focused low energy protons ( $\sim 100$  keV) which can cause short term increases in background count rates are not seen while the instrument is stowed and in general produce few events in the reject rate channel. This is further demonstrated by the good agreement in reject rates between the stowed and science observations after scaling.

<sup>\*</sup> One particle interaction can potentially create many associated events in the CCD, so there is not a one-to-one correspondence between particle rate and reject rate, but the two quantities should be related.

<sup>†</sup> The DROP\_AMP column of the level 1 exposure statistics file, “acisf\*stat1.fits”, found in the “secondary” directory ([https://cxc.cfa.harvard.edu/ciao/threads/intro\\_data/](https://cxc.cfa.harvard.edu/ciao/threads/intro_data/)).

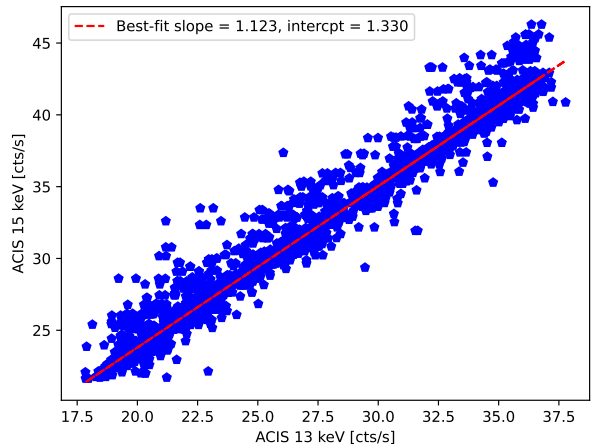


**Figure 1.** Correlation between the reject rates for the 15 keV and 13 keV pulseheight filters of ACIS data. Red line shows the best-fit linear regression.

### 2.3. XMM-Newton EPIC-pn

The EPIC-pn CCD camera stands as a key instrument on XMM-Newton, featuring a collection area of approximately  $2500 \text{ cm}^2$  at 1 keV and a field of view spanning  $27.2 \times 26.2$  degrees across the wide energy spectrum of 0.1 keV to 12 keV (Strüder et al. 2001). EPIC-pn consists of four individual quadrants (BI) each having three CCD subunits with a format  $200 \times 64$  pixels with a pixel size of  $150 \mu\text{m}$ . Operating in a highly elliptical orbit like Chandra (with an apogee of about 114,000 km and a perigee of about 7000 km), XMM-Newton also offers an environment for studying GCR interactions, relevant to upcoming X-ray telescopes’ orbits. The significance of XMM-Newton is twofold: its EPIC-pn camera bears similarity to Athena-WFI; its elliptical orbit remains unshielded by Earth’s magnetic field for the majority of its trajectory, causing it to encounter the effects of high-energy GCRs resembling Athena’s L1/L2 orbit situation (Marelli et al. 2021; Bulbul et al. 2020; Gastaldello et al. 2022).

The EPIC background encompasses three primary components: first, the background originating from detector noise and defects; second, the component resulting from mirror concentration (comprising X-ray photons and low-energy protons); and third, the unfocused high-energy particles and their subsequent products (Freyberg et al. 2004; Fraser et al. 2014; Marelli et al. 2021). For this work, we primarily focused on the unfocused component. Certain particles, such as MIPs, are identified and subsequently discarded onboard the satellite. This leads to time-dependent exclusion of CCD columns and/or events exhibiting patterns inconsistent

with valid X-ray events, primarily due to uneven spatial distribution across nearby pixels.

For this present study, we collected onboard excluded EPIC-pn CCD columns due to MIPs, known as Number of Discarded Lines (NDSLIN), as a proxy for high-energy GCR particle rates seen by EPIC-pn ‡. The EPIC-pn data used in this work was taken when telescope was in normal science operation mode and performed in Full Window Mode (FWM). We analyze all the archival EPIC-pn data in FWM mode spanning 2011–2020. Initially, EPIC-pn event files were generated and filtered using SAS tool – `epchain` and `pn-filter`. Finally, the NDSLIN rates were derived from the house-keeping extension contained within the EPIC-pn event files.

### 3. RESULTS

We present our findings obtained through the analysis and comparison of AMS proton flux, ACIS high-energy reject rates, and PN NDSLIN rates spanning the period from 2011 to 2020.

#### 3.1. Correlation between AMS, ACIS, and PN

To facilitate comparison across all three datasets, we have first re-binned them into 27-day intervals, commonly referred to as Bartel’s rotation. Within the data, outliers correspond to distinct solar storms that led to heightened particle rates. Our primary interest lies in investigating quiescent variations, prompting us to remove the positive outliers during the binning process. To detect and remove the outliers, we implemented a  $3\text{-}\sigma$  clipping method for the ACIS and EPIC-pn reject rates. Each 27-day bin was carefully examined, and count rates exceeding  $3\text{-}\sigma$  from the median value of the respective bin were flagged as anomalous and subsequently removed. However, negative outliers were not removed, as they indicate extended declines in particle background following intense solar events (Forbush 1937). Figure 2 illustrates the outcome of this 27-day binning for the AMS, ACIS, and EPIC-pn datasets. Each panel incorporates  $1\sigma$  uncertainties, although they might not be clearly visible due to their small size (comprising both statistical and systematic errors for AMS, and solely statistical errors for ACIS and PN). Despite differences in uncertainties and being plotted on different y-ranges, all three datasets exhibit noticeable degrees of similar features characteristic of the solar cycle, encompassing a significant portion of Solar Cycle 23 and a smaller fraction of Cycle 24.

To further underscore this correlation, we have employed linear regression to model relationships between the ACIS reject rates and AMS proton flux, as well as between the EPIC-pn NDSLIN rates and AMS proton flux. Figure 3 provides a visualization of these datasets along with their corresponding best-fit linear regression lines ( $\chi^2/\text{dof} = 43.6/111$  for EPIC-pn and  $\chi^2/\text{dof} = 24.8/111$  for ACIS). The computed best-fit slope for the AMS vs. ACIS fitting is 0.00273, while for the AMS vs. EPIC-pn fitting, it is 0.011. Upon extrapolation to zero AMS proton flux, the linear fits yield non-zero intercepts ACIS count rates of approximately 10 counts per second and PN count rates of roughly 44 counts per second. These non-zero intercepts are, in part, attributable to the consistent pedestal contributed by the hard X-ray background. A similar correlation between ACIS reject rates and AMS proton flux was also found by Grant et al. (2022). Notably, both linear fits exhibit high statistical significance. However, we observe minor scatter around the best-fit lines, potentially stemming from actual disparities between the two respective datasets within each time bin.

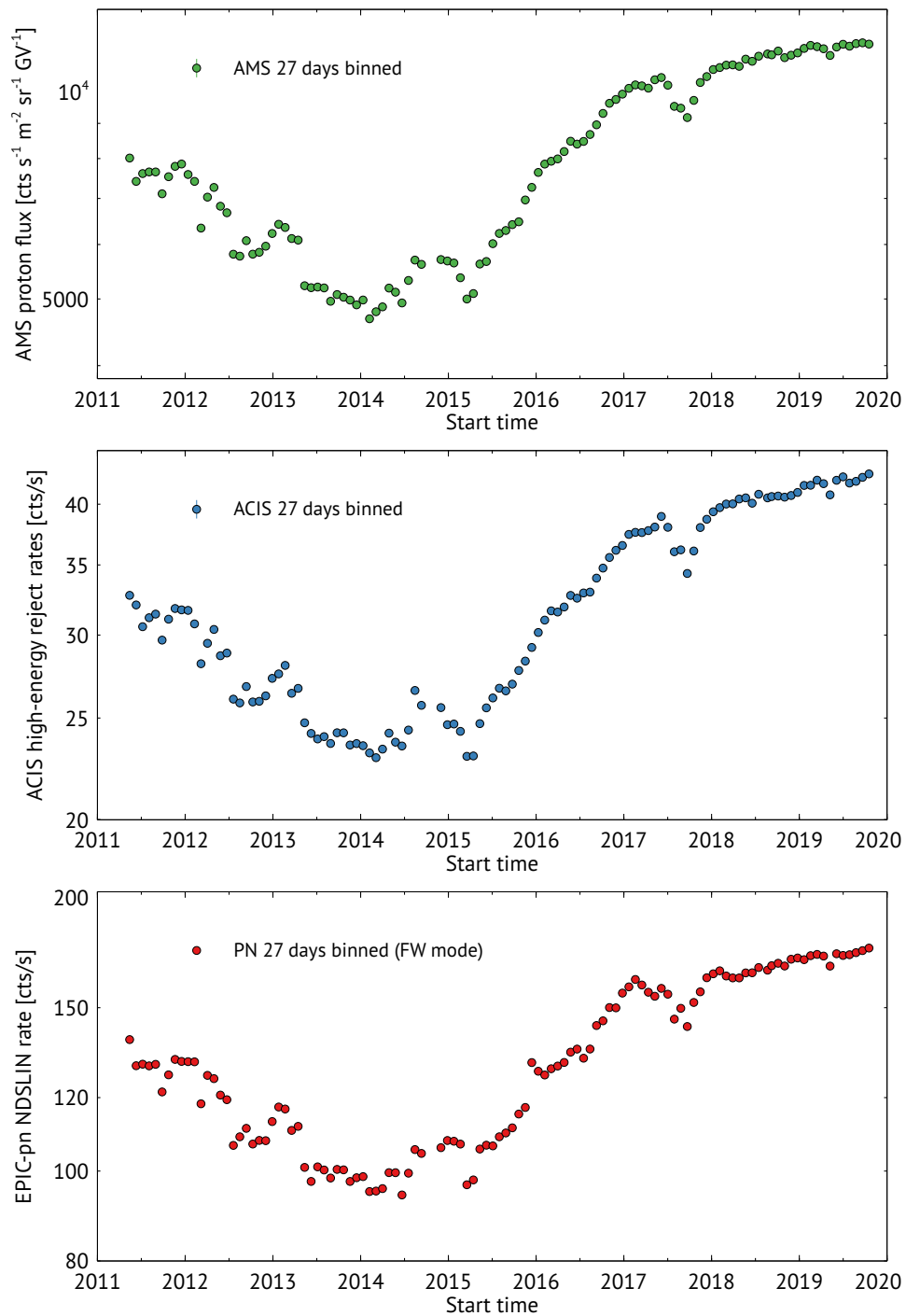
To gain a deeper insight into the factors contributing to the scatter observed in the correlation, we conducted an analysis of root mean square (RMS) deviations. Specifically, we computed the RMS deviation of the ACIS and PN data within each 27-day time bin from their respective best-fit linear regression lines. Figure 4 illustrates the resultant RMS deviations for each 27-day bin as a function of AMS proton flux. While the overall correlation remains evident, the notable magnitude of the RMS deviation underscores the existence of substantial variations within the ACIS and PN datasets occurring on timescales shorter than 27 days. This observation strongly indicates that the fluctuations in GCR particle flux exhibit finer temporal variations than the 27-day interval under consideration.

#### 3.2. Daily binned data

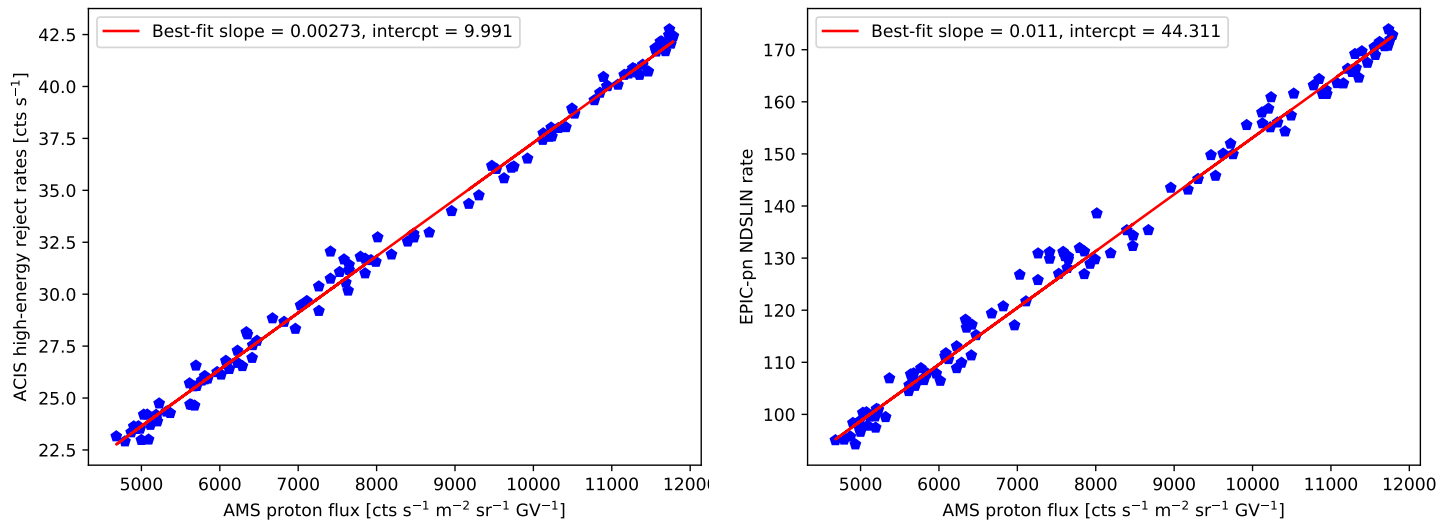
To examine the short term variation in the particle background, we re-binned the AMS proton flux, ACIS reject rates, and PN NDSLIN rates into one-day intervals. This re-binning strategy was chosen to align with the minimal time bin of one day provided by publicly released AMS data, ensuring consistency and facilitating direct comparisons across datasets. Additionally, for a comprehensive comparison of all three datasets, we re-normalized the ACIS and PN rates to match the AMS proton flux. This normalization was achieved using the best-fit slopes and intercepts as outlined in Section 3.1.

Figure 5 visually presents the outcomes of this daily binning process for the AMS, ACIS, and PN datasets,

‡ For detailed description on NDSLIN - [https://www.cosmos.esa.int/documents/332006/623312/IdIC\\_NDSLIN\\_May2019.pdf](https://www.cosmos.esa.int/documents/332006/623312/IdIC_NDSLIN_May2019.pdf)



**Figure 2.** AMS proton flux (*top*), ACIS high-energy reject rates (*middle*), and EPIC-pn NDSLIN rates (*bottom*) binned over 27-days Bartel bin, spanning the years 2011–2020. The  $1\text{-}\sigma$  uncertainties are plotted, but are too small to see.



**Figure 3.** Correlation between 27-day binned datasets. *Left:* ACIS high-energy reject rates as a function of AMS proton flux. *Right:* EPIC-pn NDSLIN rates as a function of AMS proton flux. The best-fit line is shown in red.

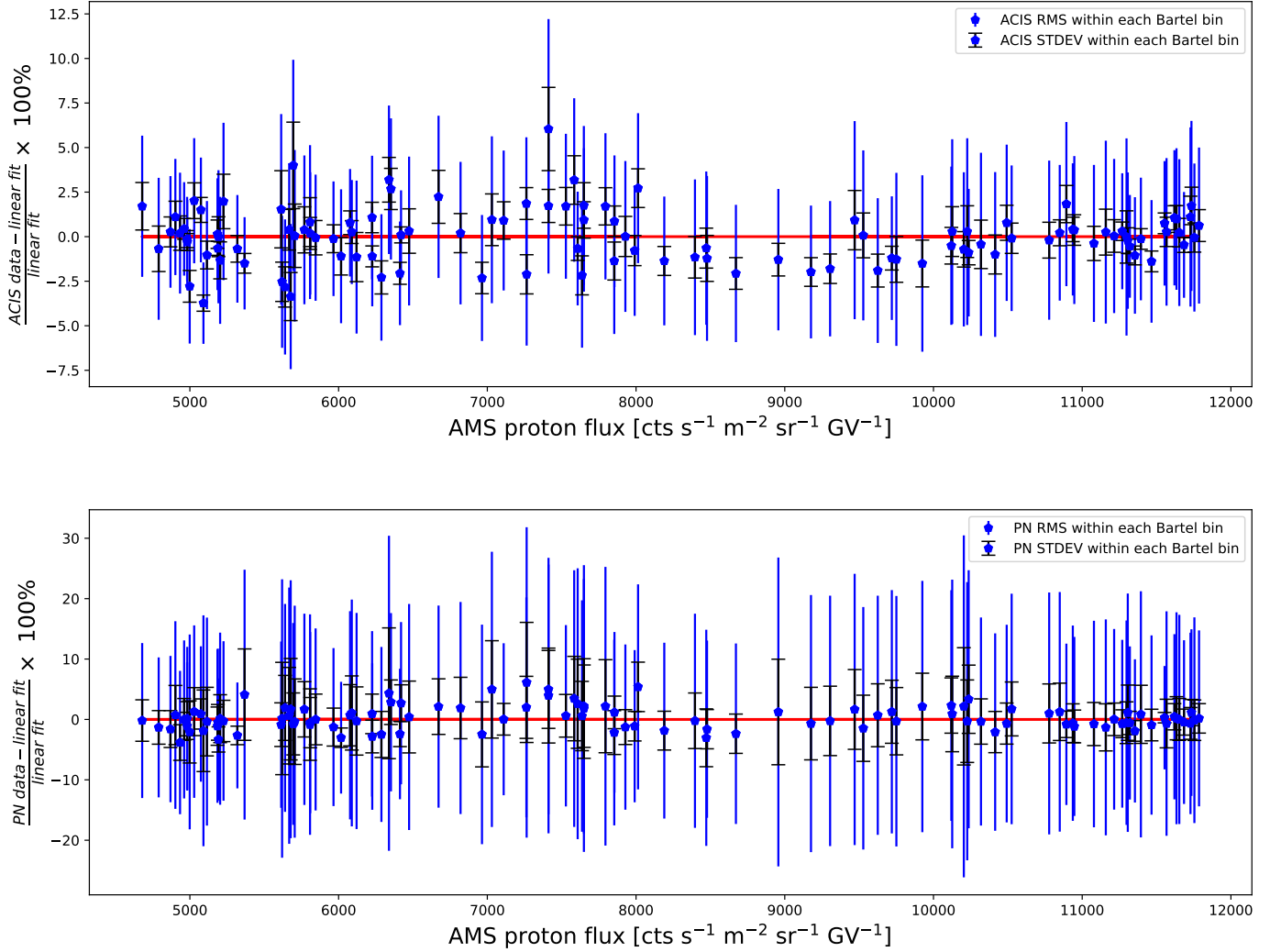


**Figure 4.** *Top:* the difference between the ACIS high-energy reject rates and the best-fit line as a function of the AMS proton flux. Both datasets were binned over 27-days. The black uncertainties on each data points represent the intrinsic scatter in ACIS data within each 27-day bin. The blue uncertainties represent RMS scatter of ACIS data within each 27-day bin *Bottom:* similar to the *Top*., but between PN NDSLIN rates and AMS proton flux.

encompassing the timeframe from 2011 to 2020. Each panel is accompanied by  $1\sigma$  uncertainties, although their visual clarity may be hindered by their relatively small size. For AMS data, these uncertainties encompass both statistical and systematic errors, whereas for ACIS and PN data, they solely encompass statistical errors. In handling outliers within individual datasets, we adopt a methodology similar to that elaborated upon in the previous section.

As expected from the AMS data, the ACIS and pn data exhibit statistically significant variations on one-day time scales. This difference is highlighted in Figure 5, where the ACIS and PN datasets exhibit greater dispersion than the AMS dataset. This discrepancy can be

attributed, in part, to the inherent characteristics of the respective instruments. AMS functions as a precision GCR particle detector, while ACIS and PN tally the count of events surpassing a specific energy threshold, acting as a proxy for the direct detection of GCR particles. Consequently, a single GCR particle can trigger multiple events (ranging from 1 to around 100) in ACIS and PN, leading to intrinsic scattering in these datasets (Miller et al. 2022). Despite this inherent scattering, all three datasets illustrate notably similar temporal variations. As depicted in Figure 6, we present the temporal variation of AMS proton flux, ACIS reject rates, and PN NDSLIN rates spanning the years 2016 to 2017. Evidently, all three datasets exhibit a consistent saw-



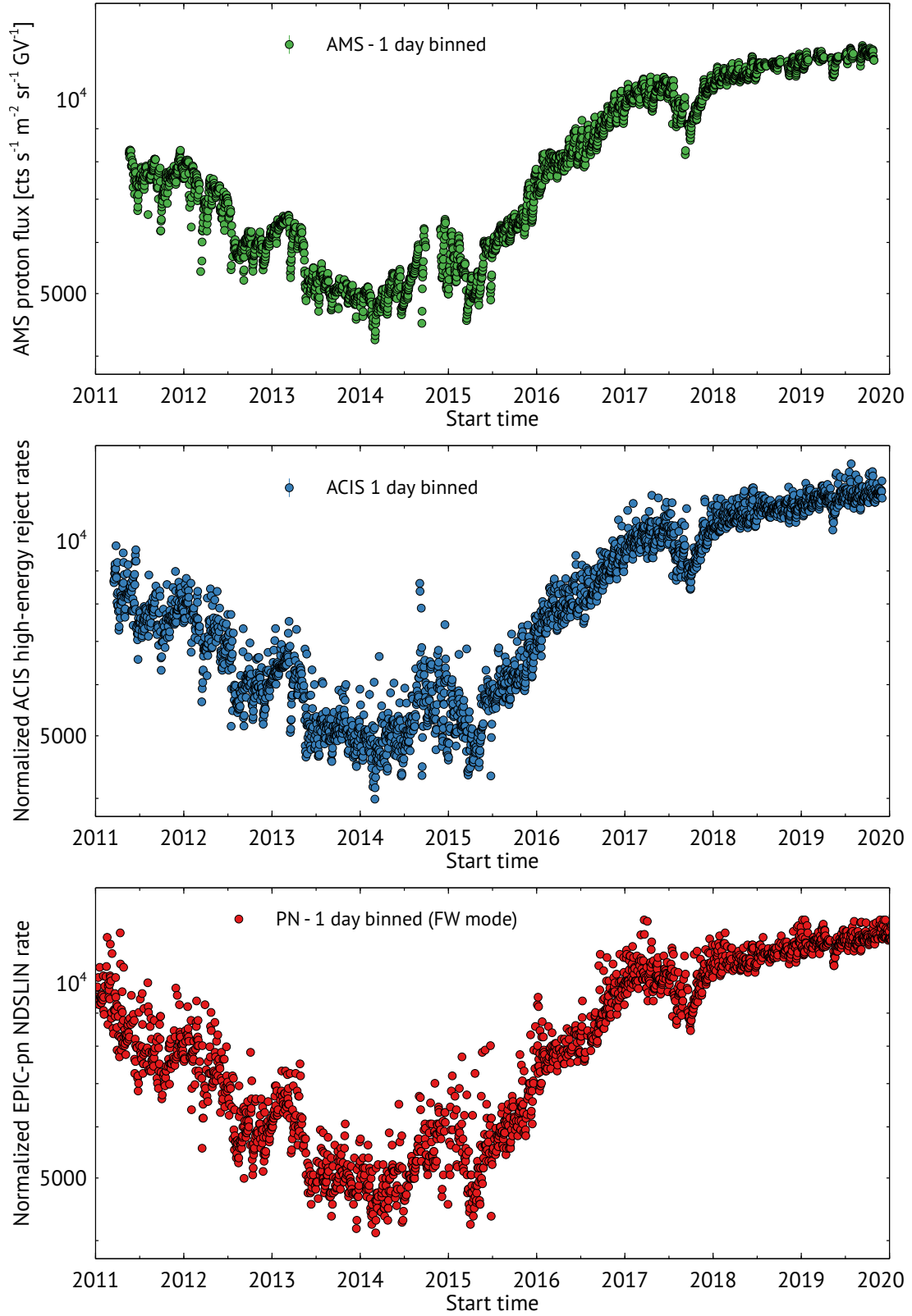


**Figure 5.** AMS proton flux, (*top*) ACIS high-energy reject rates (*middle*), and EPIC-pn NDSLIN rates (*bottom*) binned over one-day, spanning the years 2011–2020. ACIS reject rates and EPIC-pn NDSLIN rates were re-normalized to match AMS proton flux based on best-fit parameters reported in Section 3.1. The  $1\text{-}\sigma$  uncertainties are plotted, but are too small to see.

tooth pattern characterized by comparable amplitudes and frequencies. This observation clearly demonstrates that day-to-day variations in cosmic ray flux produce corresponding variation in the instrumental background.

### 3.3. Periodicity in datasets

The propagation of GCR particles from the interstellar medium through the heliosphere is substantially influenced by the large-scale solar wind flow and the turbulent interplanetary magnetic field (IMF), collectively referred to as “solar modulation”. Parker’s transport equation (Parker 1965) includes four principal modulation mechanisms, encompassing gradient and curvature drifts, diffusion within the irregular IMF, radial convection in the expanding solar wind, and adiabatic deceleration (or adiabatic energy loss) (e.g., Sabbah 2000; Ihongo & Wang 2016; Modzelewska & Gil 2021). These modulation processes intricately shape the temporal fluctuations evident in GCR particle fluxes, and thus in principle play a role in modulating instrumental backgrounds.

To investigate temporal variations across the broadest range of timescales, our search focus on the 1-day binned datasets. As illustrated in Figure 5, the global GCR particle flux exhibits a minimum between 2014 and 2015, with peaks before 2011 and around 2019. This long-term variability can be attributed to the modulation of GCR particle fluxes, driven by the magnetic polarity reversal of the Sun’s orientation (Fu et al. 2021). The 22-year helio-magnetic cycle, known as the Hale cycle, leads to a distinctive cosmic-ray intensity profile characterized by alternating sharp and flat-topped features (McDonald et al. 2010), as seen in Figure 5. This periodic pattern has been extensively examined in the literature since the early 1960s, as exemplified by studies such as McDonald et al. (2010) and references therein.

Previous studies employing daily-binned data have shown short-term (ranging from months to even days) variability in AMS proton fluxes spanning the years 2014 to 2018 (Aguilar et al. 2021), as partially depicted in Figure 6. This variability is particularly pronounced for lower energies, specifically those less than approximately 10 GeV, where the heliosphere’s magnetic shielding effect becomes crucial. To probe similar fluctuations within the ACIS and PN reject rates over shorter timescales, we have employed the wavelet time-frequency technique, as described in Torrence & Compo (1998) and Grinsted et al. (2004). A similar approach was also employed by Aguilar et al. (2021) while investigating periodicities in AMS proton flux. Figure 7 visually presents the resultant wavelet power spectra for the daily-binned AMS proton flux, ACIS and PN reject

rates, encompassing both the 2014–2018 and 2016–2017 year periods. All power spectra featured in subsequent figures are normalized by the peak value to effectively portray the strength of the underlying periodicities.

Aguilar et al. (2021) observed recurrent AMS proton flux variations with a period of  $\sim 27$  days at a significance above the 95% confidence level from 2014 to 2018. Shorter periods of  $\sim 13.5$  days and  $\sim 9$  days were also found only in 2016. Both of these periodicities are clearly visible in the top panels of Figure 7. We have identified a periodicity of  $\sim 25$  days in ACIS high-energy reject rates and a periodicity of  $\sim 23$  days in PN NDSLIN rates within the 2014–2018 timeframe, as seen in the middle-left and bottom-left panels of Figure 7. Discrepancies in these periods compared to AMS observations are primarily attributed to intrinsic scattering present in the ACIS and PN datasets leading to choosing different peaks in the datasets, as described in Section 3.2.

This recurring 27-day variation in GCR particle flux was also observed on Earth by neutron monitors (NMs; Modzelewska & Alania 2013), in space by Advanced Composition Explorer (ACE; Leske et al. 2013), out of the ecliptic plane by Ulysses (McKibben et al. 1995), and even in the remote heliosphere by the Voyager spacecraft (Decker 1999). These observations point to the solar rotation as the dominant factor driving the 27-day variability in GCR particle flux. The uneven distribution of active regions on the Sun’s surface lead to (heliographic) longitudinal asymmetry in electromagnetic conditions throughout one solar rotation, thereby modulating the 27-day wave observed in GCR particle fluxes (e.g., Richardson 2004, 2018; Modzelewska & Gil 2021).

Furthermore, we have also identified a  $\sim 9$ -day and  $\sim 13.5$ -day variability in the ACIS and PN reject rates within the 2016–2017 interval, similar to the patterns observed in AMS data, as shown in the right panels of Figure 7. These 13.5-day and 9-day periodicities correspond to the higher harmonics of the  $\sim 27$ -day GCR particle flux periodicity. Specifically, the 13.5-day periodicity represents the second harmonic, and the 9-day periodicity represents the third harmonic (Richardson 2004; Sabbah & Kudela 2011; Modzelewska & Alania 2013). The quasi-period of  $\sim 13.5$  days originates mainly due to two distinct groups of active regions on the Sun’s surface, situated approximately 180 degrees apart in longitude (Modzelewska & Alania 2013). This second harmonic has been meticulously explored by Mursula & Zieger (1996).

Furthermore, Sabbah & Kudela (2011) showed that the effects of corotating interaction regions, stemming from high-speed solar wind streams overtaking preced-

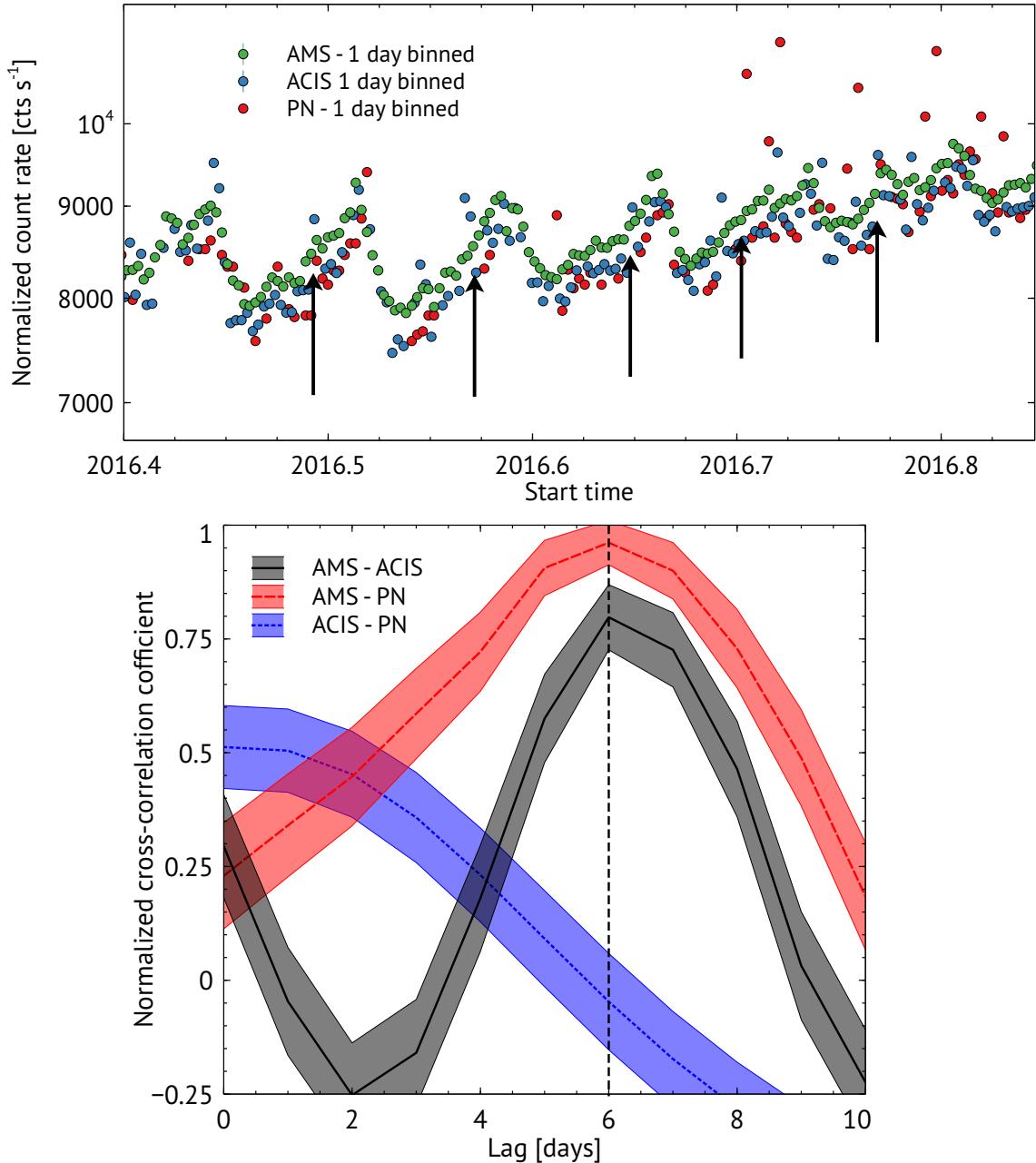


**Figure 6.** *Top:* one-day binned AMS proton flux, normalized ACIS high-energy reject rates, and normalized PN NDSLIN rates spanning the years 2016–2017. The time lag of  $\sim 6$ -days between AMS and ACIS/PN is marked by black arrows. *Bottom:* presents the cross-correlations of AMS–ACIS, AMS–EPIC-pn, and ACIS–EPIC-pn reject rates with  $1\sigma$  uncertainties, respectively, in the similar time-frame as top panel. X-axis shows the time lag between two respective data-sets. The 6-days lag has been marked with vertical dashed line.

ing slower solar wind, give rise to the 9-day GCR modulations. Comparable variability of  $\sim 13.5$  days and 9 days has also been observed in Helios 1, Helios 2, and IMP-8 experiments (Richardson 2004), Neutron Monitors (Sabbah & Kudela 2011), as well as by LISA Pathfinder (Grimani et al. 2017, 2020). These consistent findings highlight the robust nature of the observed periodicities in the ACIS and PN reject rates.

### 3.4. Time lag between datasets

We have identified a time lag of  $\sim 6$  days between AMS proton flux and ACIS/EPIC-pn reject rates. This time lag exhibits greater prominence within the time span of 2016–2017, while it becomes less apparent prior to 2016 and subsequent to 2017. Figure 6 top panel provides a visual representation of this time-lag during the 2016–2017 period, indicated by black arrows. To

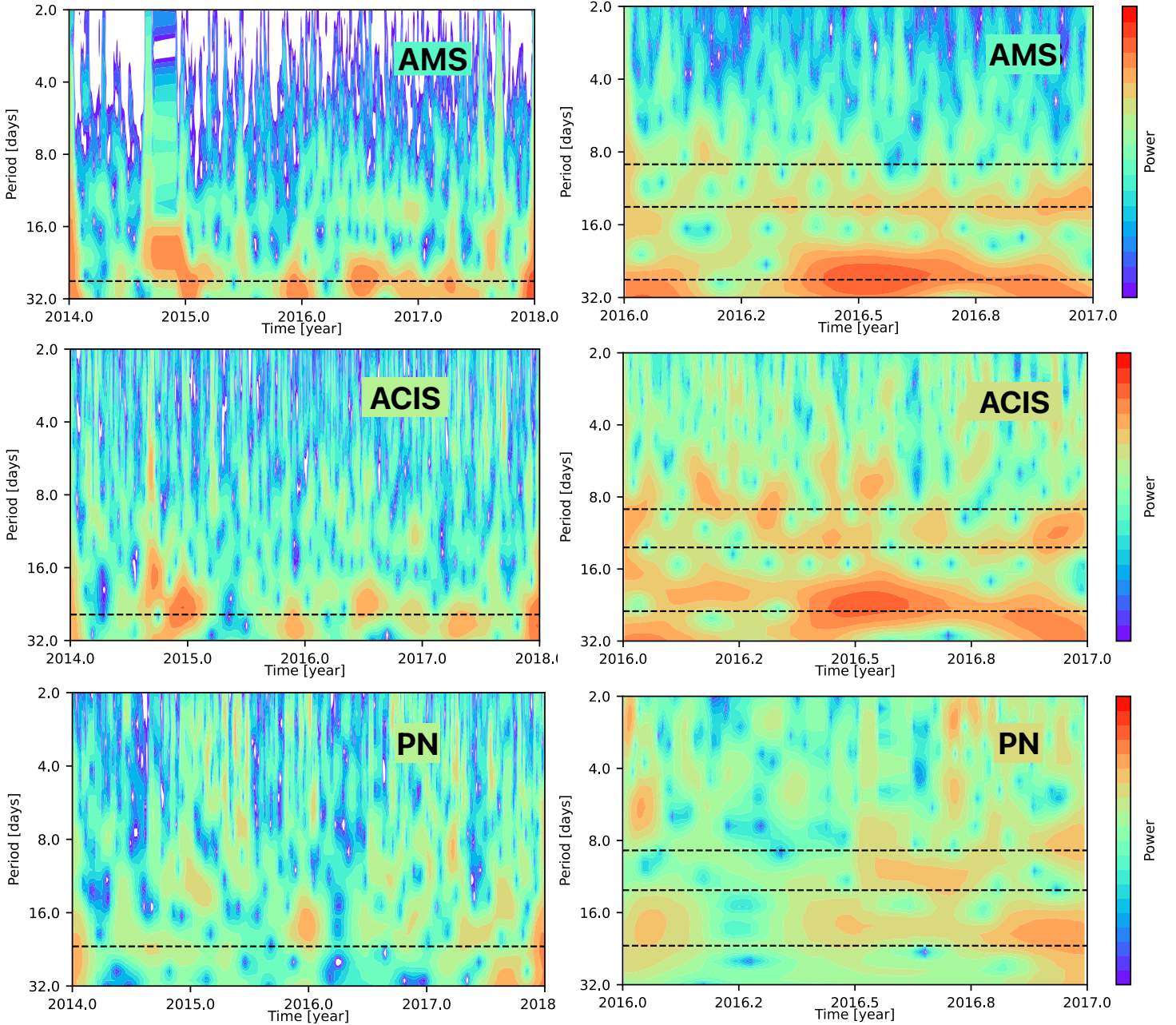


**Figure 7.** *Left panels (top to bottom):* the wavelet time-frequency power spectrum of one-day binned AMS proton fluxes, ACIS high energy reject rates, and PN NDSLIN rates, respectively, spanning in the years 2014–2018. The colorbar indicates the normalized power. The horizontal dashed lines indicate the 27 days, 25 days and 23 days periods seen in AMS, ACIS, and PN datasets, respectively. *Right panels:* similar to the left panels, but zoomed in the year span 2016–2017. The horizontal dashed lines indicate the 13.5 days, 9 days periods.

quantify the time-lag, we estimate the cross-correlations between AMS proton flux and ACIS/EPIC-pn reject rates. The bottom panels of Figure 6 display the normalized cross-correlation coefficients and the corresponding time-lag with  $1\sigma$  standard errors (SE). The standard errors were estimated adopting,  $SE = \sqrt{\frac{1-r^2}{n}}$  (Bonett 2008), where  $r$  is cross-correlation coefficient and  $n$  is

number of data points. A distinct time-lag of 6 days is evident in both cross-correlations, corroborating our observations from the top panel of Figure 6. The underlying cause of this observed time lag remains uncertain.

To facilitate a comprehensive comparison of all three datasets, we have normalized the ACIS and EPIC-pn reject rates to align with the AMS proton flux using the best-fit parameters obtained from the linear fit pre-

sented in Figure 3. This normalization process may introduce slight short-term scaling discrepancies in count rates. This arises due to the fact that the linear fitting was executed on 27-day binned data, leading to a visual impression of a time lag. It is important to emphasize that this lag is specifically evident on the ascending portions of the curve, as depicted in Figure 6, and is most noticeable in the second half of 2016. Notably, within a similar time span, ACIS and EPIC-pn reject rates align with each other without any noticeable lag, despite being measured by different instruments and being scaled independently. We show in the bottom panel of Figure 6 that ACIS and EPIC-pn reject rates cross-correlates best with no time lag. These observations suggest that the observed time lag may not solely be attributed to the scaling factor.

#### 4. DISCUSSION

A fundamental objective of forthcoming X-ray observatories is the mapping the cosmic web through deep exposures of faint diffuse sources. Achieving this science goal hinges on maintaining low and well-determined background levels and a comprehensive understanding of the residual unrejected background. Notably, the predominant contributor to the particle background at energy levels surpassing 1-2 keV is attributed to GCR protons. As described in the preceding section, the fluxes and spectrum of GCR protons exhibit modulation patterns related to both the 11-year solar cycle and shorter temporal scales characterized by spans of months, weeks, or even days due to solar activity. The principal objective of this paper centers on the understanding this variability in various locations in space, notably those situated at L1/L2, which may prove crucial to minimizing uncertainties in particle-background of ESA’s NewAthena X-ray Observatory and other missions with large collecting area, like Lynx (Gaskin et al. 2019), Advanced X-ray Imaging Satellite (AXIS; Mushotzky et al. 2019), and Line Emission Mapper (LEM; Kraft et al. 2022).

Particle background data used in analyzing faint diffuse X-ray sources is often derived from the extended observations ( $> 100$  ks) of relatively blank part of the sky and dark Moon (Bartalucci et al. 2014). However, a common challenge arises from the temporal disparity between the blank-sky observation date and the actual observation of the science target. The underlying assumption is that the particle background remains stable at the high elliptical orbit at any subsequent time post the blank-sky observation. We have shown that the substantial variability of the GCR particle flux, on time scale as short as 1 day, produces corresponding variations in the

background observed in the X-ray imaging instruments (as seen in Figure 4). An important question is, therefore, the reliability of a background measurement obtained at a specific time ‘ $t$ ’ for utilization with a science observation at a later time. To answer this question, we have estimated the auto-correlation of AMS proton flux, ACIS and EPIC-pn reject rates starting from an arbitrarily selected date. The auto-correlation function offers a relative measure of the correlation between data at time  $t = 0$  and any subsequent time.

For each of the datasets, we computed the auto-correlation between measurements at the initial day ( $t=0$ ) and subsequent days. Figure 8 presents the resulting auto-correlation functions for all three datasets. Notably, the AMS dataset maintains a significant correlation percentage exceeding 70% even after 6 days from its initial measurement at  $t=0$ . However, the auto-correlation percentages for the ACIS and EPIC-pn reject rates exhibit a rapid decline compared to AMS. Specifically, for the ACIS dataset, the auto-correlation drops below 60% by the 5th day, while for the EPIC-pn dataset, it falls below 50% on the subsequent day following the start-point.

We investigated whether the inherent fluctuations in the ACIS and EPIC-pn reject rates are the main cause of the quicker decay observed in their auto-correlations compared to the AMS. To explore this, we introduced random Gaussian noise mimicking scatter in the ACIS and EPIC-pn reject rates to the AMS proton flux and computed the auto-correlation within the same timeframe. The auto-correlation of the AMS proton flux with added noise, illustrated by the dashed blue and green curves in Figure 8, exhibited a similarly rapid decline as observed in the EPIC-pn and ACIS reject rates. This finding confirms that the intrinsic variability in the EPIC-pn and ACIS reject rates is the primary contributor to the rapid decline in their auto-correlations. Moreover, it suggests that additional stochastic processes and sources may contribute to the variability, the mechanisms of which are not yet fully understood.

These observations pose a challenge to the conventional practice of employing blank-sky observations to constrain particle background, especially considering its misalignment with the actual date of scientific observations. This underscores the potential value of incorporating dedicated instrumentation to monitor background-generating particles in X-ray telescopes, especially operating in orbits with little or no geomagnetic shielding. However, the AMS, serving as a precision GCR particle detector, demonstrates the capacity to retain a higher correlation percentage, thereby holding potential for particle-background constraint for X-

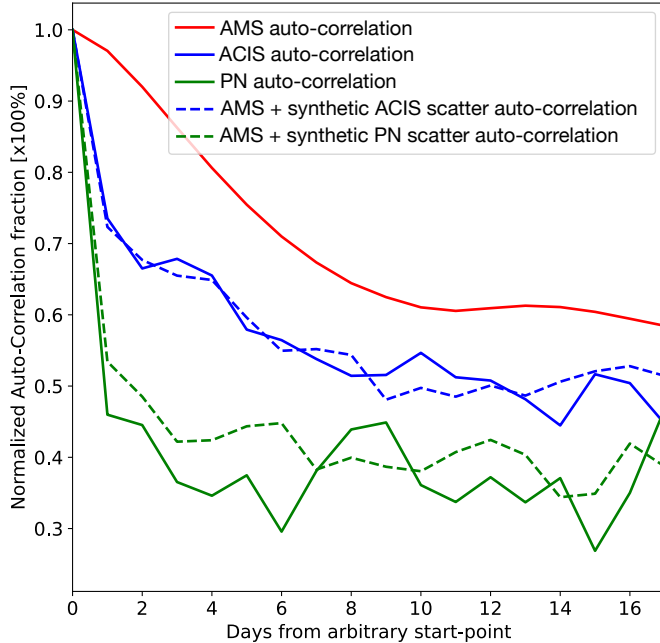


**Figure 8.** Auto-correlation functions of AMS proton flux, ACIS high-energy reject rates, and PN NDSLIN rates, estimated using one-day binned data, starting from an arbitrary date of observation. The y-axis shows the correlation percentage. Dashed blue and green curves show the auto-correlation of the AMS proton flux after adding the synthetic scatter of ACIS and PN reject rates, respectively.

ray telescopes. In an upcoming study, we will show how the AMS can effectively be utilized to predict particle background for telescopes situated in high elliptical orbits.

## 5. CONCLUSION

For the first time, we have introduced daily-binned datasets encompassing high-energy reject rates recorded by ACIS and EPIC-pn instruments, using nearly all archival science observations spanning from 2011 to 2020. These high-energy reject rates serve as proxy measurements for GCR proton fluxes, which are precisely measured by the AMS particle detector onboard the ISS. We have conducted a comprehensive comparison of the variability observed in the ACIS and EPIC-pn reject rates with that of AMS proton fluxes. Our findings are summarized below.

- We compared all three data sets binned to match the 27 day binning in the AMS data release. We find ACIS and EPIC-pn reject rates strongly correlate with the AMS proton fluxes. However, there is substantial variation in the ACIS and EPIC-pn reject rates within each Bartel time bin, indicating variability on shorter timescales. This observation strongly indicates that the fluctuations in GCR

particle flux, on shorter timescales, produces corresponding variations in the background observed in the X-ray imaging instruments.

- To understand the temporal dynamics of the GCR particles, we rebinned ACIS and PN datasets into one-day interval, similar to AMS. Daily binned datasets exhibit finer temporal structures in comparison to those binned over 27-days intervals. We note ACIS and EPIC-pn datasets display more intrinsic scattering than AMS. The excess variability in ACIS and EPIC-pn data compared to AMS is of unknown origin and may involve additional sources of instrumental background beyond those produced by GCR. While AMS directly measure the GCR proton flux, ACIS and EPIC-pn counts the events surpassing a specific energy threshold. Despite this intrinsic scattering, all three datasets show remarkably similar temporal variations with similar amplitudes and frequencies.
- All three datasets show a overall minima between 2014–2015 and peaks < 2011 and 2019. The long-term variability is due to the modulation of the GCR particle fluxes by the 11-year solar cycle. We also find recurrent ACIS and EPIC-pn reject rates vary with a period of  $\sim 25$  days and  $\sim 23$  days, respectively, in the 2014–2018 year band. Similar variation in AMS proton flux was also observed by Aguilar et al. (2021). The longitudinal asymmetry of the electro-magnetic field in the heliosphere, which arises from the uneven distribution of active regions on the Sun’s surface during a single solar rotation, modulates the 27-day period in GCR particle fluxes. Additionally, we have also detected  $\sim 13.5$  days and  $\sim 9$  days period, also known as the second and third harmonics of 27-days period, in ACIS and EPIC-pn reject rates between 2016–2017.
- A time lag of  $\sim 6$  days has been observed between AMS proton flux and ACIS/EPIC-pn reject rates in the second half of 2016. This time lag is predominantly absent before 2016 and after 2017. The underlying cause of this time lag remains largely unidentified. Nevertheless, the time lag could potentially stem from the scaling relationship between AMS and ACIS/EPIC-pn, as well as the reconstruction procedures applied to the AMS proton flux by the AMS team.

We thank anonymous referee for their helpful comments and suggestions. We are grateful to the AMS team for their thorough documentation and the public

availability of AMS data. This work was done as part of the Athena WFI Background Working Group, a consortium including MPE, INAF/IASF-Milano, IAAT, Open

University, MIT, SAO, and Stanford. We gratefully acknowledge support from NASA cooperative agreement 80NSSC21M0046 and NASA contracts NAS 8-37716 and NAS 8-38252.

## REFERENCES

- Aguilar, M., Aisa, D., Alpat, B., et al. 2015, *PhRvL*, 114, 171103, doi: [10.1103/PhysRevLett.114.171103](https://doi.org/10.1103/PhysRevLett.114.171103)
- Aguilar, M., Ali Cavasonza, L., Alpat, B., et al. 2018, *PhRvL*, 121, 051101, doi: [10.1103/PhysRevLett.121.051101](https://doi.org/10.1103/PhysRevLett.121.051101)
- Aguilar, M., Cavasonza, L. A., Ambrosi, G., et al. 2021, *PhRvL*, 127, 271102, doi: [10.1103/PhysRevLett.127.271102](https://doi.org/10.1103/PhysRevLett.127.271102)
- Bartalucci, I., Mazzotta, P., Bourdin, H., & Vikhlinin, A. 2014, *A&A*, 566, A25, doi: [10.1051/0004-6361/201423443](https://doi.org/10.1051/0004-6361/201423443)
- Bazilevskaya, G., Broomhall, A. M., Elsworth, Y., & Nakariakov, V. M. 2014, *SSRv*, 186, 359, doi: [10.1007/s11214-014-0068-0](https://doi.org/10.1007/s11214-014-0068-0)
- Bonett, D. G. 2008, *Psychological Methods*, 13, 173–181, doi: [10.1037/a0012868](https://doi.org/10.1037/a0012868)
- Boschini, M. J., Della Torre, S., Gervasi, M., et al. 2017, *ApJ*, 840, 115, doi: [10.3847/1538-4357/aa6e4f](https://doi.org/10.3847/1538-4357/aa6e4f)
- Bulbul, E., Kraft, R., Nulsen, P., et al. 2020, *ApJ*, 891, 13, doi: [10.3847/1538-4357/ab698a](https://doi.org/10.3847/1538-4357/ab698a)
- Campana, R. 2022, in *Handbook of X-ray and Gamma-ray Astrophysics*, 39, doi: [10.1007/978-981-16-4544-0\\_28-1](https://doi.org/10.1007/978-981-16-4544-0_28-1)
- Chowdhury, P., Kudela, K., & Moon, Y. J. 2016, *SoPh*, 291, 581, doi: [10.1007/s11207-015-0832-7](https://doi.org/10.1007/s11207-015-0832-7)
- Decker, R. 1999, in *International Cosmic Ray Conference*, Vol. 7, 26th International Cosmic Ray Conference (ICRC26), Volume 7, 512
- Forbush, S. E. 1937, *Physical Review*, 51, 1108, doi: [10.1103/PhysRev.51.1108.3](https://doi.org/10.1103/PhysRev.51.1108.3)
- Fraser, G. W., Read, A. M., Sembay, S., Carter, J. A., & Schyns, E. 2014, *MNRAS*, 445, 2146, doi: [10.1093/mnras/stu1865](https://doi.org/10.1093/mnras/stu1865)
- Freyberg, M. J., Briel, U. G., Dennerl, K., et al. 2004, in *Society of Photo-Optical Instrumentation Engineers (SPIE) Conference Series*, Vol. 5165, *X-Ray and Gamma-Ray Instrumentation for Astronomy XIII*, ed. K. A. Flanagan & O. H. W. Siegmund, 112–122, doi: [10.1117/12.506277](https://doi.org/10.1117/12.506277)
- Fu, S., Zhang, X., Zhao, L., & Li, Y. 2021, *ApJS*, 254, 37, doi: [10.3847/1538-4365/abf936](https://doi.org/10.3847/1538-4365/abf936)
- Gaskin, J. A., Swartz, D. A., Vikhlinin, A., et al. 2019, *Journal of Astronomical Telescopes, Instruments, and Systems*, 5, 021001, doi: [10.1117/1.JATIS.5.2.021001](https://doi.org/10.1117/1.JATIS.5.2.021001)
- Gastaldello, F., Ghizzardi, S., Marelli, M., et al. 2017, *Experimental Astronomy*, 44, 321, doi: [10.1007/s10686-017-9549-y](https://doi.org/10.1007/s10686-017-9549-y)
- Gastaldello, F., Marelli, M., Molendi, S., et al. 2022, *ApJ*, 928, 168, doi: [10.3847/1538-4357/ac5403](https://doi.org/10.3847/1538-4357/ac5403)
- Grant, C. E., Bautz, M. W., & Virani, S. N. 2002, in *Astronomical Society of the Pacific Conference Series*, Vol. 262, *The High Energy Universe at Sharp Focus: Chandra Science*, ed. E. M. Schlegel & S. D. Vrtilik, 401, doi: [10.48550/arXiv.astro-ph/0202086](https://doi.org/10.48550/arXiv.astro-ph/0202086)
- Grant, C. E., Miller, E. D., Bautz, M. W., et al. 2018, in *Society of Photo-Optical Instrumentation Engineers (SPIE) Conference Series*, Vol. 10699, *Space Telescopes and Instrumentation 2018: Ultraviolet to Gamma Ray*, ed. J.-W. A. den Herder, S. Nikzad, & K. Nakazawa, 106994H, doi: [10.1117/12.2313864](https://doi.org/10.1117/12.2313864)
- Grant, C. E., Miller, E. D., Bautz, M. W., et al. 2022, in *Society of Photo-Optical Instrumentation Engineers (SPIE) Conference Series*, Vol. 12181, *Space Telescopes and Instrumentation 2022: Ultraviolet to Gamma Ray*, ed. J.-W. A. den Herder, S. Nikzad, & K. Nakazawa, 121812E, doi: [10.1117/12.2629520](https://doi.org/10.1117/12.2629520)
- Grimani, C., Cesarini, A., Fabi, M., et al. 2020, *ApJ*, 904, 64, doi: [10.3847/1538-4357/abbb90](https://doi.org/10.3847/1538-4357/abbb90)
- Grimani, C., LISA Pathfinder Collaboration, Benella, S., et al. 2017, in *Journal of Physics Conference Series*, Vol. 840, *Journal of Physics Conference Series*, 012037, doi: [10.1088/1742-6596/840/1/012037](https://doi.org/10.1088/1742-6596/840/1/012037)
- Grinsted, A., Moore, J. C., & Jevrejeva, S. 2004, *Nonlinear Processes in Geophysics*, 11, 561, doi: [10.5194/npg-11-561-2004](https://doi.org/10.5194/npg-11-561-2004)
- Ihongo, G. D., & Wang, C. H. T. 2016, *Ap&SS*, 361, 44, doi: [10.1007/s10509-015-2628-5](https://doi.org/10.1007/s10509-015-2628-5)
- Kouline, A. 2012, *International Journal of Modern Physics E*, 21, 1230005, doi: [10.1142/S0218301312300056](https://doi.org/10.1142/S0218301312300056)
- Kraft, R., Markevitch, M., Kilbourne, C., et al. 2022, *arXiv e-prints*, arXiv:2211.09827, doi: [10.48550/arXiv.2211.09827](https://doi.org/10.48550/arXiv.2211.09827)
- Kudela, K., & Sabbah, I. 2016, *Science in China E: Technological Sciences*, 59, 547, doi: [10.1007/s11431-015-5924-y](https://doi.org/10.1007/s11431-015-5924-y)
- Kuntz, K. D., & Snowden, S. L. 2008, *A&A*, 478, 575, doi: [10.1051/0004-6361:20077912](https://doi.org/10.1051/0004-6361:20077912)

- Leske, R. A., Cummings, A. C., Mewaldt, R. A., & Stone, E. C. 2013, *SSRv*, 176, 253, doi: [10.1007/s11214-011-9772-1](https://doi.org/10.1007/s11214-011-9772-1)
- Lumb, D. H., Warwick, R. S., Page, M., & De Luca, A. 2002, *A&A*, 389, 93, doi: [10.1051/0004-6361:20020531](https://doi.org/10.1051/0004-6361:20020531)
- Marelli, M., Molendi, S., Rossetti, M., et al. 2021, *ApJ*, 908, 37, doi: [10.3847/1538-4357/abcfbc](https://doi.org/10.3847/1538-4357/abcfbc)
- McDonald, F. B., Webber, W. R., & Reames, D. V. 2010, *Geophys. Res. Lett.*, 37, L18101, doi: [10.1029/2010GL044218](https://doi.org/10.1029/2010GL044218)
- McKibben, R. B., Simpson, J. A., Zhang, M., Bame, S., & Balogh, A. 1995, *SSRv*, 72, 403, doi: [10.1007/BF00768812](https://doi.org/10.1007/BF00768812)
- Miller, E. D., Grant, C. E., Bautz, M. W., et al. 2022, *Journal of Astronomical Telescopes, Instruments, and Systems*, 8, 018001, doi: [10.1117/1.JATIS.8.1.018001](https://doi.org/10.1117/1.JATIS.8.1.018001)
- Modzelewska, R., & Alania, M. V. 2013, *SoPh*, 286, 593, doi: [10.1007/s11207-013-0261-4](https://doi.org/10.1007/s11207-013-0261-4)
- Modzelewska, R., & Gil, A. 2021, *A&A*, 646, A128, doi: [10.1051/0004-6361/202039651](https://doi.org/10.1051/0004-6361/202039651)
- Molendi, S. 2017, *Experimental Astronomy*, 44, 263, doi: [10.1007/s10686-017-9544-3](https://doi.org/10.1007/s10686-017-9544-3)
- Mursula, K., & Zieger, B. 1996, *J. Geophys. Res.*, 101, 27077, doi: [10.1029/96JA02470](https://doi.org/10.1029/96JA02470)
- Mushotzky, R., Aird, J., Barger, A. J., et al. 2019, in *Bulletin of the American Astronomical Society*, Vol. 51, 107, doi: [10.48550/arXiv.1903.04083](https://doi.org/10.48550/arXiv.1903.04083)
- Nandra, K., Barret, D., Barcons, X., et al. 2013, arXiv e-prints, arXiv:1306.2307, doi: [10.48550/arXiv.1306.2307](https://doi.org/10.48550/arXiv.1306.2307)
- Parker, E. N. 1965, *SSRv*, 4, 666, doi: [10.1007/BF00216273](https://doi.org/10.1007/BF00216273)
- Poliszczuk, A., Wilkins, D., Allen, S. W., et al. 2023, in *Applications of Machine Learning 2023*, ed. M. E. Zelinski, T. M. Taha, J. Howe, & B. N. Narayanan, Vol. 12675, International Society for Optics and Photonics (SPIE), 126750C, doi: [10.1117/12.2677095](https://doi.org/10.1117/12.2677095)
- Potgieter, M. S. 2013, *Living Reviews in Solar Physics*, 10, 3, doi: [10.12942/lrsp-2013-3](https://doi.org/10.12942/lrsp-2013-3)
- Reynolds, C., Kara, E., Mushotzky, R. F., & Ptak, A. 2023, in *Society of Photo-Optical Instrumentation Engineers (SPIE) Conference Series*, Vol. 12678, Optics + Photonics 2023: UV, X-Ray, and Gamma-Ray Space Instrumentation for Astronomy XXIII, 12678–49
- Richardson, I. G. 2004, *SSRv*, 111, 267, doi: [10.1023/B:SPAC.0000032689.52830.3e](https://doi.org/10.1023/B:SPAC.0000032689.52830.3e)
- . 2018, *Living Reviews in Solar Physics*, 15, 1, doi: [10.1007/s41116-017-0011-z](https://doi.org/10.1007/s41116-017-0011-z)
- Sabbah, I. 2000, *Geophys. Res. Lett.*, 27, 1823, doi: [10.1029/2000GL003760](https://doi.org/10.1029/2000GL003760)
- Sabbah, I., & Kudela, K. 2011, *Journal of Geophysical Research (Space Physics)*, 116, A04103, doi: [10.1029/2010JA015922](https://doi.org/10.1029/2010JA015922)
- Sarkar, A., Su, Y., Randall, S., et al. 2021, *MNRAS*, 501, 3767, doi: [10.1093/mnras/staa3858](https://doi.org/10.1093/mnras/staa3858)
- Sarkar, A., Su, Y., Truong, N., et al. 2022a, *MNRAS*, 516, 3068, doi: [10.1093/mnras/stac2416](https://doi.org/10.1093/mnras/stac2416)
- Sarkar, A., Randall, S., Su, Y., et al. 2022b, *ApJL*, 935, L23, doi: [10.3847/2041-8213/ac86d4](https://doi.org/10.3847/2041-8213/ac86d4)
- . 2023, *ApJ*, 944, 132, doi: [10.3847/1538-4357/aca9f](https://doi.org/10.3847/1538-4357/aca9f)
- Sarkar, A., Andrade-Santos, F., van Weeren, R. J., et al. 2024, *ApJ*, 962, 161, doi: [10.3847/1538-4357/ad1aac](https://doi.org/10.3847/1538-4357/ad1aac)
- Strüder, L., Briel, U., Dennerl, K., et al. 2001, *A&A*, 365, L18, doi: [10.1051/0004-6361:20000066](https://doi.org/10.1051/0004-6361:20000066)
- Tomassetti, N. 2017, arXiv e-prints, arXiv:1712.03178, doi: [10.48550/arXiv.1712.03178](https://doi.org/10.48550/arXiv.1712.03178)
- Torrence, C., & Compo, G. P. 1998, *Bulletin of the American Meteorological Society*, 79, 61, doi: [10.1175/1520-0477\(1998\)079<0061:APGTWA>2.0.CO;2](https://doi.org/10.1175/1520-0477(1998)079<0061:APGTWA>2.0.CO;2)
- Usoskin, I. G. 2017, *Living Reviews in Solar Physics*, 14, 3, doi: [10.1007/s41116-017-0006-9](https://doi.org/10.1007/s41116-017-0006-9)
- von Kienlin, A., Eraerds, T., Bulbul, E., et al. 2018, in *Society of Photo-Optical Instrumentation Engineers (SPIE) Conference Series*, Vol. 10699, Space Telescopes and Instrumentation 2018: Ultraviolet to Gamma Ray, ed. J.-W. A. den Herder, S. Nikzad, & K. Nakazawa, 106991I, doi: [10.1117/12.2311987](https://doi.org/10.1117/12.2311987)
- Weisskopf, M. C., Tananbaum, H. D., Van Speybroeck, L. P., & O'Dell, S. L. 2000, in *Society of Photo-Optical Instrumentation Engineers (SPIE) Conference Series*, Vol. 4012, X-Ray Optics, Instruments, and Missions III, ed. J. E. Truemper & B. Aschenbach, 2–16, doi: [10.1117/12.391545](https://doi.org/10.1117/12.391545)